processes

IMPACT FACTOR 3.4

CITESCORE 5.7

Article

Hierarchical Sensitivity Analysis of PV Converter Operating Profiles Under Climatic and Grid Uncertainty

Ivelina Hinova, Silvia Baeva and Mirjana Kocaleva Vitanova

Special Issue
Adaptive Control and Optimization in Power Grids

Edited by
Dr. Xiaoping Xiong, Dr. Fanrong Wei and Dr. Lingling Xie

MDPI

https://doi.org/10.3390/pr14162677

processes

MDPI

Article

Hierarchical Sensitivity Analysis of PV Converter Operating Profiles Under Climatic and Grid Uncertainty

Ivelina Hinova [1,*], Silvia Baeva [2] and Mirjana Kocaleva Vitanova [3]

[1] Department of Management and business information systems, Faculty of Management, Technical University of Sofia, 1000 Sofia, Bulgaria
[2] Department of Mathematical Modelling and Numerical Methods, Faculty of Applied Mathematics and Informatics, Technical University of Sofia, 1000 Sofia, Bulgaria; sbaeva@tu-sofia.bg
[3] Department of Applied Mathematics, Faculty of Computer Science, Goce Delcev University, Stip, North Macedonia; mirjana.kocaleva@ugd.edu.mk
* Correspondence: ihinova@tu-sofia.bg

Abstract

Photovoltaic converters operate under varying climatic conditions and non-ideal grid regimes, but factor importance is often assessed either through isolated local metrics or through pooled operating data that hide regime shifts and interaction effects. This study develops a hierarchical framework for sensitivity analysis of operating profiles of grid-connected PV converters under climatic and grid uncertainty. A compact operating-profile formulation is introduced that relates solar radiation, cell and ambient temperature, grid voltage, load, and selected design/control parameters to active power, efficiency, power factor, harmonic distortion, DC bus ripple, clipping behavior, and thermal headroom. The proposed workflow combines local normalized sensitivities for fast ranking around nominal conditions, Morris screening for factor reduction, and Sobol/Saltelli variance-based indices for global prioritization under uncertainty. The framework is demonstrated on a 100 kW synthetic reduced-order benchmark representing a three-phase two-level grid-connected PV inverter with an LCL filter. To clarify the scope of validity, the reduced-order model is cross-checked against switching-level simulations for representative nominal, clipping-prone, high-temperature and grid-stress operating windows. The results show that factor importance is not universal, but depends on the selected KPI, operating regime and uncertainty scenario. In the considered benchmark, grid voltage, cell temperature and equivalent thermal resistance are the dominant total-effect contributors, while the strongest second-order contribution appears between grid voltage and filter inductance under grid-stress conditions. The proposed framework is therefore intended as a reproducible, regime-aware sensitivity workflow rather than as a universal ranking of PV converter parameters.

Keywords: PV converter; sensitivity analysis; Morris screening; Sobol/Saltelli indices; quantitative uncertainty assessment; operating profile; power quality; thermal headroom

Academic Editor: Jiaqiang E

Received: 13 May 2026
Revised: 29 June 2026
Accepted: 30 June 2026
Published: 21 August 2026

1. Introduction

1.1. Relevance of the Topic

Photovoltaic (PV) systems have become one of the leading technologies for renewable electricity generation, and the grid-connected converter is the component that links energy conversion, grid-code compliance, power quality, reliability and controllability. In modern PV plants, the inverter is not only a DC/AC interface, but it also participates

 https://doi.org/10.3390/pr14162677

in voltage/reactive-power support, synchronization, current control, harmonic filtering, protection, and monitoring [1–5].

The design of a power-electronic converter is usually performed around a nominal operating point. In field operation, however, the same converter is exposed to variable irradiance, cell and ambient temperatures, load levels, grid voltage, and grid frequency. These variations change the active-power injection, conversion efficiency, power factor (PF), total harmonic distortion (THD), DC-link ripple and thermal reserve. Consequently, the importance of a design or control factor cannot be treated as a fixed property of the converter; it must be interpreted together with the operating regime and with the uncertainty model used for the analysis.

From a methodological perspective, sensitivity analysis provides a structured means of identifying which uncertain inputs control model responses and where nonlinear or interaction effects become important. Morris introduced factorial sampling plans based on elementary effects for the preliminary screening of computational models [6], while Campolongo et al. improved this screening strategy to distinguish influential factors more effectively at a moderate computational cost [7]. These approaches are well suited to PV-converter studies involving many climatic, grid, design and control inputs because they can reduce the factor set before a more computationally demanding global analysis.

Variance-based global sensitivity analysis provides a complementary quantitative decomposition of output uncertainty. Sobol formulated first-order and higher-order sensitivity indices for nonlinear models [8], and Saltelli et al. subsequently proposed an efficient sampling design and estimator for total-effect indices [9]. The broader methodological framework presented by Saltelli et al. [10] clarifies the distinction between factor prioritization, factor fixing and interaction assessment, whereas Pianosi et al. [11] emphasize that the selected sensitivity measure must be aligned with the modeling purpose, uncertainty assumptions and intended decision. Together, these studies support a hierarchical workflow in which local derivatives, Morris screening and Sobol/Saltelli indices answer different, but mutually complementary, engineering questions.

For grid-connected PV converters, sensitivity results must also be interpreted within accepted power-quality and monitoring frameworks. IEEE Std 519-2022 defines the harmonic-assessment context at the point of common coupling [12], while IEC 61724-1:2021 specifies terminology, measurement and monitoring principles for PV-system performance [13]. In parallel, the open-source SALib environment provides documented implementations of Morris and Sobol/Saltelli procedures and therefore supports transparent sampling, repeatable calculations and explicit reporting of analysis settings [14]. These elements are important for distinguishing a reproducible sensitivity study from a ranking derived from undocumented preprocessing or proprietary calculations.

At the system and converter levels, recent reviews demonstrate that PV performance is governed by a combination of architecture, control, environment and operational practice. Morey et al. summarize grid-connected PV architectures, control structures and ancillary-service functions [15], whereas Abdulla et al. identify operation and maintenance requirements that connect performance deviations with inspection and lifecycle decisions [16]. Bamisile et al. review the environmental variables affecting PV output, including irradiance and temperature-related effects [17], and Hossain et al. synthesize recent developments in grid-connected inverter topologies and control techniques [18]. This body of work confirms that the converter should be evaluated over a multidimensional operating profile rather than only at a single nominal point.

The need for regime-dependent analysis becomes more pronounced when grid support and reliability are included. Saedabad et al. show that weak-grid conditions can alter harmonic stability in solar power plants [19]. Brito et al. demonstrate that reactive-power capability and inverter sizing involve a reliability-related trade-off [20], while Chai et al. assess PV-inverter operational reliability when voltage/VAR control is active [21]. Mission-profile studies further indicate that the definition of thermal loading affects the reliability evaluation of power devices [22], and diagnostic research links inverter health to cooling-path and air-duct condition [23]. Accordingly, grid stress, reactive-power demand and thermal derating should be treated as distinct operating regimes because they can change both KPI values and the relative importance of the governing factors.

Uncertainty and nonlinear operating constraints add a further layer to this problem. Zhang et al. analyze uncertainty in PV-cell parameters in relation to the probability of functional failure [24] and subsequently apply global sensitivity analysis to quantify the influence of PV-cell parameters under credibility-based variance treatment [25]. Micheli et al. show that inverter clipping changes performance and loss signatures, including the interpretation of soiling-related effects [26]. These findings imply that a factor ranking calculated from pooled data may conceal changes that occur specifically during clipping, derating, part-load or grid-stress intervals.

Reproducible benchmarking also depends on representative data, explicit quality control and accessible computational tools. Fleet-level loss analysis provides evidence on availability and performance-loss factors across operating PV systems [27], and open reliability datasets create a basis for independent method comparison [28]. Climate-specific field assessments further show that degradation and fault trends vary across environmental zones [29]. The pvlib Python ecosystem supports transparent PV modeling [30], and its data-access functions facilitate reproducible acquisition and preprocessing of solar-resource information [31]. These resources motivate the explicit reporting of input distributions, segmentation rules, software versions and random seeds.

Finally, the engineering value of sensitivity analysis depends on how its results are connected to KPI quality, reliability and diagnostic decisions. Lindig et al. review technical PV KPIs and demonstrate the importance of data-quality routines [32], while an international collaboration framework stresses uniform calculation procedures, benchmarks and quality controls for performance-loss rates [33]. Recent studies propose fast inverter reliability assessment [34], machine-learning-based predictive modeling and anomaly detection [35], and cost-effective data-driven fault detection and diagnosis for distributed PV systems [36]. Collectively, this literature establishes the need for a workflow that not only ranks uncertain factors, but also explains how their importance changes across operating regimes and how the resulting ranking can support design, monitoring and maintenance.

This study treats the operating profile as a multidimensional object that combines climatic inputs, grid conditions, design/control variables, active operating regimes, KPI trajectories and admissible operating limits. These groups of factors are presented in Table 1. The formulation provides a common mathematical structure for local, screening and global sensitivity analysis.

Table 1. Main groups of factors and KPIs used in the operating profile formulation.

Group	Designations	Representative Quantities	Role in the Analysis
Climate inputs	G, T_c, T_{amb}	irradiance, cell temperature, ambient temperature	Determines available PV power, temperature-dependent losses and thermal stress
Grid inputs	V_g, f_g	grid voltage and frequency	Affect synchronization, PF, THD_I, voltage/reactive-power control and operating limits
Operating point	λ, $m(t)$	relative loading and active mode	Links climatic/grid states to nominal, part-load, clipping, derating or grid-stress operation

Table 1. *Cont.*

Group	Designations	Representative Quantities	Role in the Analysis
Design/control parameters	$f_s, L_f, C_f, R_{\mathrm{th,eq}}, k_{\mathrm{MPPT}}, ILR$	switching frequency, filter, equivalent thermal path, MPPT gain, DC/AC ratio	Determine losses, harmonic attenuation, thermal reserve, clipping and control response
Output KPIs	$P_{AC}, Q_{AC}, \eta, PF, THD_I, r_{VDC}, C_{\mathrm{clip}}, HT$	active/reactive power, efficiency, power factor, current THD, DC ripple, clipping, thermal headroom	Minimum set for design, control tuning, monitoring, maintenance and benchmark comparison

1.2. Scientific Gap and Research Objectives

Despite extensive work on PV modeling, power electronics, and sensitivity analysis, four gaps remain relevant. First, local sensitivity measures are often used alone and therefore remain valid only near a selected operating point. Second, global sensitivity indices are frequently reported on pooled annual data, where nominal, part-load, clipping, derating and grid-stress intervals are mixed into one statistical ensemble. Third, the generating converter model, uncertainty distributions, preprocessing rules and random seeds are often incompletely reported. Fourth, sensitivity rankings are rarely connected to a reproducible reporting package that permits cross-study comparison.

To address these gaps, the operating profile is compactly represented as

$$\mathcal{P} = \{x(t), \theta, m(t), y(t), \mathcal{D}, \mathcal{U}, K_{\min}\}, \tag{1}$$

where $x(t)$ contains climate and grid inputs, θ contains converter design and control parameters, $m(t)$ denotes the active operating regime, $y(t)$ contains instantaneous and aggregated KPIs, $\mathcal{D}$ is the admissible operating domain, $\mathcal{U}$ is the uncertainty model, and $K_{\min}$ is the minimum reporting KPI package.

The objective of this paper is to develop and demonstrate a reproducible, hierarchical workflow for regime-aware sensitivity analysis of PV converter operating profiles under climatic and grid uncertainty.

1.3. Research Questions and Contributions

The study is guided by the following research questions:

RQ1. Which factors dominate the main PV converter KPIs under local and global sensitivity analysis?

RQ2. How does factor importance change between nominal, part-load, clipping, thermal derating, and grid-stress regimes?

RQ3. Does the sequential use of local sensitivity, Morris screening, and Sobol/Saltelli indices provide additional engineering information compared with a single local or pooled global ranking?

The main contributions are as follows:

- A compact operating-profile representation linking climate, grid, design/control variables, operating regimes, and KPIs;
- A regime-aware hierarchical sensitivity workflow combining local, Morris, and Sobol/Saltelli indices;
- A reproducible synthetic benchmark specification, including the reduced-order generating model, uncertainty distributions, segmentation rules, random seed, and software settings;
- An engineering interpretation layer connecting sensitivity results with design, control tuning, monitoring, predictive maintenance, and benchmark-ready reporting.

A scheme of the workflow with hierarchical sensitivity is presented in Figure 1.

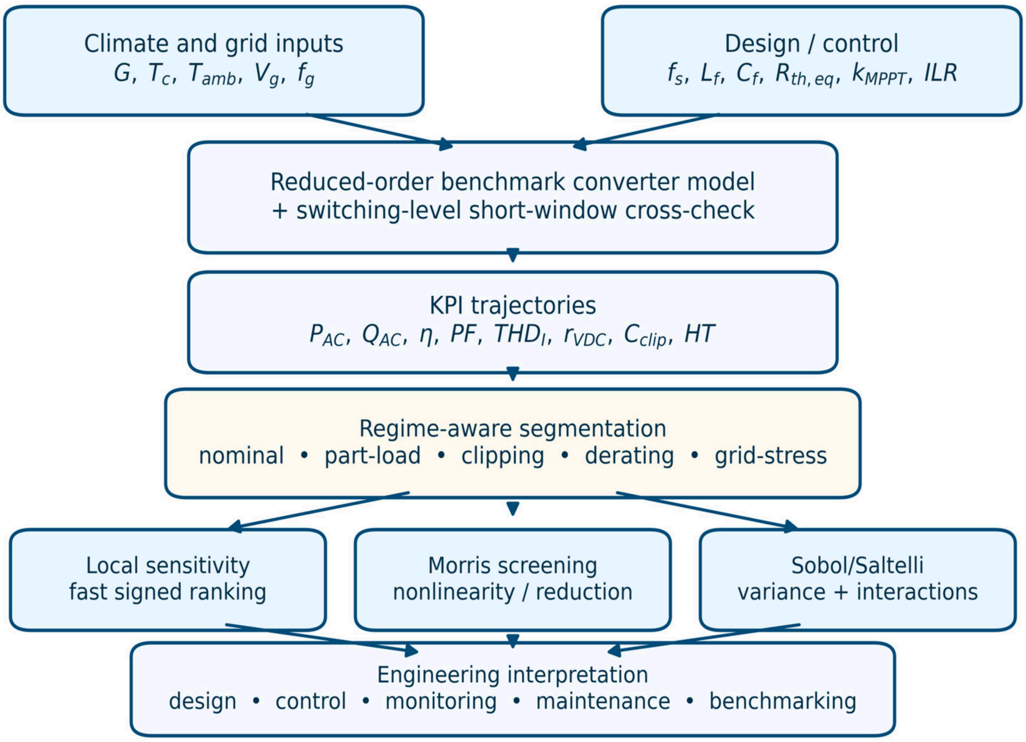

Figure 1. Regime-aware, hierarchical sensitivity workflow for PV converter operating-profile analysis. Blue boxes denote model and analysis stages, arrows indicate information flow, and the pale-yellow box marks the regime-segmentation step.

2. Materials and Methods

2.1. Compact Mathematical Formulation of the Operating Profile

The observed time interval is $t \in [0, T]$. The converter behavior is represented by the general state-space form

$$\dot{s}(t) = f(s(t), x(t), \theta, m(t)), \tag{2}$$

$$y(t) = h(s(t), x(t), \theta, m(t)), \tag{3}$$

where $s(t)$ is the vector of internal states, $x(t)$ is the input vector, θ is the parameter vector, $m(t)$ is the operating mode, and $y(t)$ is the vector of output KPIs. The input vector is

$$x(t) = \left[G(t), T_c(t), T_{\text{amb}}(t), V_g(t), f_g(t), \lambda(t)\right]^T, \tag{4}$$

where $G(t)$ is the effective solar radiation, $T_c(t)$ is the cell or module temperature, $T_{\text{amb}}(t)$ is the ambient temperature, $V_g(t)$ is the grid voltage, $f_g(t)$ is the grid frequency, and $\lambda(t)$ is the normalized load or equivalent operating point indicator, and the design/control parameter vector is

$$\theta = \left[f_s, L_f, C_f, R_{\text{th,eq}}, k_{\text{MPPT}}, ILR, \theta_{\text{prot}}\right]^T, \tag{5}$$

where f_s is the switching frequency, L_f and C_f are LCL filter parameters, $R_{\text{th,eq}}$ is the calibrated equivalent junction-to-ambient thermal parameter, k_{MPPT} represents the MPPT dynamic gain, ILR is the inverter loading ratio or DC/AC ratio, and θ_{prot} summarizes the derating and protection logic.

The output vector is defined as

$$y(t) = [P_{AC}(t), Q_{AC}(t), \eta(t), PF(t), THD_I(t), r_{VDC}(t), HT(t)]^T, \tag{6}$$

where $P_{AC}(t)$ and $Q_{AC}(t)$ are the active and reactive power of the AC side, $\eta(t)$ is the instantaneous efficiency, $PF(t)$ is the power factor, $THD_I(t)$ is the total harmonic distortion, $r_{VDC}(t)$ is the relative ripple of the DC bus, and $HT(t)$ is the thermal headroom.

The notation THD_I is used to denote current total harmonic distortion at the inverter output/PCC. Voltage THD is treated as a grid-stress indicator and not as the main converter KPI.

The power factor and current harmonic distortion are calculated as

$$PF(t) = \frac{P_{AC(t)}}{\sqrt{P_{AC}^2(t) + Q_{AC}^2(t)}}, \tag{7}$$

$$THD_I(t) = \frac{\sqrt{\sum_{n=2}^{N_h} I_n^2(t)}}{I_1(t)}, \quad N_h = 50 \tag{8}$$

The upper harmonic order $N_h = 50$ is consistent with the steady-state harmonic-assessment range used for PCC-oriented power-quality evaluation in IEEE Std 519-2022 [12].

The relative DC-link ripple over a local window of N samples is

$$r_{VDC}(t) = \frac{\sqrt{\left(\frac{1}{N}\right)\sum_{k=1}^{N}\left(V_{DC}[k] - \bar{V}_{DC}\right)^2}}{\bar{V}_{DC}}, \tag{9}$$

where $\overline{V}_{DC}$ is the average value of the DC bus voltage in the considered window.

$$HT(t) = T_{j,\max} - T_j(t), \tag{10}$$

where $T_{j,\max}$ is the maximum allowable junction temperature.

2.2. Reduced-Order Benchmark Converter Model

The annual benchmark results are generated using a reduced-order converter model rather than a switching-level simulation over the full yearly horizon. The model is intended to preserve the dominant steady-state dependencies between irradiance, temperature, loading, grid voltage, filtering parameters, losses, harmonic distortion, and thermal headroom, while remaining computationally feasible for Morris and Sobol/Saltelli sampling.

The available PV-side DC power is calculated as

$$P_{PV,\mathrm{av}}(t) = P_{\mathrm{DC,STC}}\frac{G(t)}{G_{\mathrm{STC}}}\left[1 + \gamma_P(T_c(t) - 25\ ^\circ\mathrm{C})\right], \tag{11}$$

where $P_{\mathrm{DC,STC}} = ILR \cdot P_{\mathrm{rated}}$, $G_{\mathrm{STC}} = 1000\ \mathrm{W/m^2}$, and $\gamma_P = -2.62 \times 10^{-3}{\cdot}\mathrm{K}^{-1}$ is the module power temperature coefficient. This calibrated coefficient gives $P_{\mathrm{PV,av}} = 93.98$ kW at $G = 850\ \mathrm{W/m^2}$, $T_c = 55\ ^\circ\mathrm{C}$ and $ILR = 1.20$.

$$\tau_{\mathrm{MPPT}}(k_{\mathrm{MPPT}})\frac{dP_{\mathrm{MPPT}}}{dt} + P_{\mathrm{MPPT}} = P_{\mathrm{PV,av}}, \tag{12}$$

$$\tau_{\mathrm{MPPT}} = \tau_{\mathrm{MPPT,0}}\frac{k_{\mathrm{MPPT,0}}}{k_{\mathrm{MPPT}}}, \quad \tau_{MPPT,0} = 5\ \mathrm{s} \tag{13}$$

$$P_{\mathrm{cmd}}(t) = \lambda(t)P_{\mathrm{rated}}, \tag{14}$$

$$P_{AC}^*(t) = \max[0, P_{\mathrm{MPPT}}(t) - P_{\mathrm{loss}}(t)], \tag{15}$$

$$AC(t) = \min\left[P_{AC}^*(t),\ P_{\mathrm{cmd}}(t),\ P_{\mathrm{rated}},\ P_{\mathrm{der}}(T_j)\right] \tag{16}$$

$$P_{AC}(t) = \min\left[\eta_{\text{conv}}(t)P_{\text{PV,av}}(t), P_{\text{rated}}, P_{\text{der}}(T_j)\right] \tag{17}$$

Equations (12)–(17) give k_{MPPT} an explicit dynamic role. At the 1 min annual time step, the MPPT state is updated with the exact first-order discrete solution. Its influence is therefore small for quasi-steady KPIs but remains available for transient extensions.

The derating function is defined as

$$P_{\text{der}}(T_j) = \begin{cases} P_{\text{rated}}, & T_j < T_{\text{der}} \\ P_{\text{rated}}\left(1 - \frac{T_j - T_{\text{der}}}{T_{j,\max} - T_{\text{der}}}\right), & T_{\text{der}} \le T_j < T_{j,\max} \\ 0, & T_j \ge T_{j,\max} \end{cases} \tag{18}$$

The total converter loss is represented as the sum of conduction, switching, filter and auxiliary losses:

$$P_{\text{loss}}(t) = P_{\text{cond}}(t) + P_{\text{sw}}(t) + P_{\text{filter}}(t) + P_{\text{aux}}, \tag{19}$$

with the coupled power, reactive-power, loss and thermal equations:

$$P_{\text{cond}} = a_c\lambda^2\left(\frac{I_{AC}}{I_{AC,\text{ref}}}\right)^2\left[1 + \alpha_T(T_j - T_{j,0})\right], \; P_{\text{sw}} = a_s\lambda\frac{f_s}{f_{s,0}}, \; P_{\text{filter}} = a_f\lambda^2\left(\frac{I_{AC}}{I_{AC,\text{ref}}}\right)^2\frac{L_{f,0}}{L_f}, \tag{20}$$

are solved at each sample by fixed-point iteration with a tolerance of 10^{-6} kW and a maximum of 20 iterations, where:

$$I_{AC}(t) = \frac{\sqrt{P_{AC}^2(t) + Q_{AC}^2(t)}}{\sqrt[3]{V_g(t)}}, \qquad I_{AC,\text{ref}}(\lambda) = \lambda\frac{P_{\text{rated}}}{\sqrt[3]{V_{\text{nom}}}PF_{\text{ref}}} \tag{21}$$

Equations (19)–(21) introduce the physically required grid-voltage and reactive-power dependence of conduction and filter losses.

The conversion efficiency is then evaluated only during active operation.

$$\eta(t) = \frac{P_{AC}(t)}{P_{AC}(t) + P_{\text{loss}}(t)}, \qquad P_{AC}(t) > P_{\min} = 0.05\,P_{\text{rated}} \tag{22}$$

Efficiency is not reported for inactive or near-zero-power intervals because the ratio is dominated by standby or numerical auxiliary losses. This masking rule prevents physically meaningless non-zero efficiency values at zero output power.

The cell temperature is generated by a first-order thermal response rather than by instantaneous tracking of irradiance:

$$\tau_T\frac{dT_c}{dt} + T_c = T_{\text{amb}} + c_T G + \epsilon_T, \qquad c_T = 0.028\ ^\circ\text{C}, \qquad \epsilon_T \sim N\left(0, 2.5^2\right) \tag{23}$$

with $G_0 = 850\ \text{W/m}^2$ and $T_{\text{amb},0} = 31\ ^\circ\text{C}$, the dynamic model gives $T_{c,0}$ approximately 55 °C. The nominal sensitivity point is therefore $T_{c,0} = 55\ ^\circ\text{C}$.

$$T_j(t) = T_{\text{amb}}(t) + R_{\text{th,eq}}P_{\text{loss}}(t), \qquad HT(t) = T_{j,\max} - T_j(t) \tag{24}$$

The calibrated values $R_{\text{th,eq}} = 33.5$ K/kW and $P_{\text{aux}} = 0.274$ kW give $P_{\text{loss},0}$ approximately 1.884 kW, $T_{j,0}$ approximately 94.10 °C and HT_0 approximately 30.90 °C at the nominal point. $R_{\text{th,eq}}$ is an equivalent junction-to-ambient hot-spot parameter, not a heat-sink-only resistance.

The net reactive power at the PCC is defined by a nominal PF setpoint plus a 24
bounded voltage droop contribution:

$$e_V(t) = \frac{V_g(t)}{V_{\text{nom}}} - 1, \tag{25}$$

$$Q_0(t) = P_{AC}(t)\tan\left[\arccos\left(PF_{ref}\right)\right], \tag{26}$$

$$Q_V(t) = \begin{cases} 0 \; for \; |e_V| \leq \delta_V \\ -\text{sgn}(e_V)K_Q(|e_V| - \delta_V)S_{\text{rated}} \; for \; |e_V| > \delta_V \end{cases}, \tag{27}$$

$$Q_{\text{lim}}(t) = \min\left[0.30\; S_{\text{rated}},\; \sqrt{max(S_{\text{rated}}^2 - P_{AC}^2(t), 0)}\right], \tag{28}$$

$$Q_{AC}(t) = \text{clip}[Q_0(t) + Q_V(t), -Q_{\text{lim}}(t),\; Q_{\text{lim}}(t)] \tag{29}$$

The benchmark uses $PF_{\text{ref}} = 0.992$, delta_$V = 0.02$ p.u., $K_Q = 0.90$ p.u./p.u., $S_{\text{rated}} = 110$ kVA and $Q_{max} = 33$ kVAr. These values reproduce PF approximately 0.992 at nominal voltage and PF approximately 0.983 at $V_g = 370$ V and P_{AC} approximately 90.8 kW. The LCL-capacitor contribution is included in the net PCC calibration and is quantified separately in the filter-design check below.

The reduced-order current-distortion and DC-link-ripple submodels are:

$$THD_I = THD_0\left(\frac{L_{f,0}}{L_f}\right)^{0.56}\left(\frac{f_{s,0}}{f_s}\right)^{0.27}\left(\frac{V_g}{V_{nom}}\right)^{0.33}\left(\frac{\lambda_0}{\lambda}\right)^{0.18}[1 + 11.5|e_V|]\left[1 + \frac{0.18\max(T_c - 55.0)}{15}\right] + \epsilon_H, \tag{30}$$

$$r_{VDC} = r_0\left(\frac{f_{s,0}}{f_s}\right)^{0.34}\left(\frac{\lambda}{\lambda_0}\right)^{0.28}\left(\frac{ILR}{ILR_0}\right)^{0.16}[1 + 6.0|e_V|]\left[1 + \frac{0.20\max(T_c - 55.0)}{15}\right] + \epsilon_r, \tag{31}$$

where $THD_0 = 2.6\%$, $r_0 = 1.6\%$, $\lambda_0 = 0.921$ and $ILR_0 = 1.20$. The residuals ϵ_H and ϵ_r are set to zero during deterministic sensitivity evaluation and are generated with random seed 202601 only for time-profile visualization. The equations, coefficient file, and executable functions are included in Supplementary File S1. Table 2 summarizes the calibrated coefficients used for benchmark generation.

Table 2. Calibrated reduced-order model coefficients used for benchmark generation.

Coefficient	Value	Unit/Role
γ_P	-2.62×10^{-3}	K^{-1}; PV power temperature coefficient
a_c	1.10	kW; conduction-loss coefficient
a_s	0.55	kW; switching-loss coefficient
a_f	0.20	kW; filter-loss coefficient
P_{aux}	0.274	kW; calibrated auxiliary loss
α_T	3.0×10^{-3}	K^{-1}; loss temperature coefficient
$f_{s,0}/L_{f,0}$	10/1.8	kHz/mH
λ_0/ILR_0	0.921/1.20	nominal sensitivity point
$T_{j,0}/T_{\text{der}}/T_{j,\max}$	94.0/105/125	°C
$R_{\text{th,eq}}$	33.5	K/kW
$PF_{\text{ref}}/\delta_V/K_Q$	0.992/0.02/0.90	-/p.u./p.u.-per-p.u.
$S_{\text{rated}}/Q_{\text{max}}$	110/33	kVA/kVAr
THD_0/r_0	2.6/1.6	%/%

Table 2. *Cont.*

Coefficient	Value	Unit/Role
$\tau_T/\tau_{\mathbf{MPPT,0}}$	20 min/5 s	thermal/MPPT time constants
$P_{\mathbf{min}}$	0.05 P_{rated}	efficiency reporting threshold
Random seed	202601	profile residuals and sampling reproducibility

The same values are supplied in machine-readable JSON and CSV formats in Supplementary File S1. The reduced-order model dependencies are summarized in Figure 2.

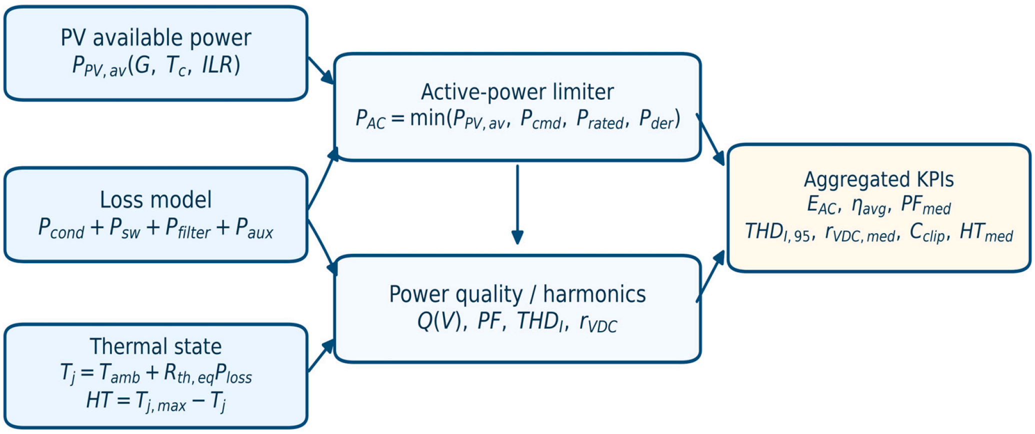

Figure 2. Reduced-order model dependencies used to generate the synthetic benchmark KPIs.

2.3. Benchmark Converter, Control Assumptions and Numerical Environment

The benchmark system is a 100 kW AC, 110 kVA, three-phase two-level grid-connected PV string inverter with a 120 kWp DC array ($ILR = 1.20$). The MPPT is represented by Equation (11), grid synchronization uses a 20 Hz SRF-PLL with zeta_PLL $= 0.707$, the inner dq-current loop has a nominal bandwidth of 1 kHz, and the outer DC-link voltage loop has a nominal bandwidth of 20 Hz. PCC monitoring supplies V_g, f_g, PF, THD_I and the optional THD_V flag used for grid-stress classification. Table 3 lists the corresponding converter, control and numerical-environment settings.

Table 3. Configuration of the benchmark converter, control assumptions, and numerical environment.

Parameter	Value/Setting
Inverter type	Three-phase two-level grid-connected string inverter with LCL filter
Rated AC power $P_{\mathbf{rated}}$	100 kW
Rated apparent power $S_{\mathbf{rated}}$	110 kVA
Nominal DC array power $P_{\mathbf{DC,STC}}$	120 kWp
DC/AC ratio/ILR	1.20
Rated AC voltage and frequency	400 V line-to-line; 50 Hz
Rated DC voltage and MPPT range	800 V; 550–950 V
MPPT representation	First-order P&O/incremental-conductance equivalent; $k_{MPPT,0} = 0.018$; $\tau_{MPPT,0} = 5$ s
Grid synchronization	SRF-PLL; bandwidth 20 Hz; damping ratio $\zeta_{PLL} = 0.707$
Inner current-control loop	Nominal closed-loop bandwidth 1 kHz
Outer DC-link voltage loop	Nominal closed-loop bandwidth 20 Hz
Reactive-power control	$Q(V)$ droop; $PF_{\text{ref}} = 0.992$; $\delta_V = 0.02$ p.u.; $K_Q = 0.90$ p.u./p.u.; $Q_{\max} = 33$ kVAr; Equations (25)–(29)

Table 3. *Cont.*

Parameter	Value/Setting
Grid monitoring at PCC	RMS voltage, frequency, PF, THD_I and optional THD_V; grid-stress rule in Section 2.4
Switching-level modulation	Space-vector PWM (SVPWM) at $f_s = 10$ kHz
Inverter-side inductance $\boldsymbol{L_1}$	1.2 mH
Grid-side inductance $\boldsymbol{L_2}$	0.6 mH
Equivalent inductance $\boldsymbol{L_f = L_1 + L_2}$	1.8 mH; $L_1 : L_2 = 2:1$ retained in the L_f sensitivity study
Filter capacitor $\boldsymbol{C_f}$	20 microF/phase
Series damping resistor $\boldsymbol{R_d}$	1.5 ohm
LCL resonance frequency $\boldsymbol{f_{res}}$	Approximately 1.78 kHz
DC-link capacitance $\boldsymbol{C_{DC}}$	5 mF
Equivalent thermal parameter $\boldsymbol{R_{th,eq}}$	33.5 K/kW
Derating start/emergency shutdown	105 °C/125 °C
Annual horizon/base time step	1 representative year/1 min
Switching cross-check settings	Fixed time step 1 microsecond; 2.0 s window; first 0.5 s discarded; remaining 1.5 s averaged
Implementation	Python 3.11.7; NumPy 1.26.4; pandas 2.2.2; SciPy 1.13.1; SALib 1.5.0; matplotlib 3.8.4
Random seed	202601

The LCL filter parameters are selected using standard current-ripple, reactive-power, and resonance-frequency constraints. The filter capacitor is limited by the reactive power injected at rated voltage:

$$Q_C = 3\omega_g C_f V_{ph}^2 \tag{32}$$

For $C_f = 20\,\mu$F and $V_{ph} = 400/\sqrt{3}$ V, $Q_C \approx 1$ kVAr, i.e., approximately 1% of the rated apparent power. With $L_1 = 1.2$ mH, $L_2 = 0.6$ mH and $C_f = 20$ microF/phase, Equation (33) gives $f_{res} \approx 1.78$ kHz, which satisfies $10 f_g = 500$ Hz $< f_{res} < 0.5 f_s = 5$ kHz. The converter/control block structure and monitored signals are shown in Figure 3.

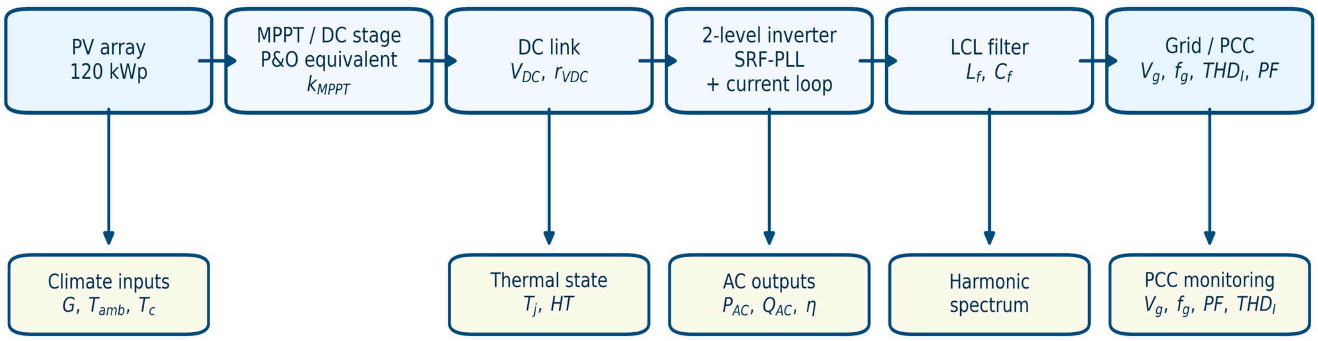

Figure 3. Benchmark converter, control blocks, and monitored PCC/DC-link signals. Blue boxes indicate power-conversion stages, and pale boxes indicate monitored input/output quantities.

The resonance frequency is checked by

$$f_{res} = \frac{1}{2\pi}\sqrt{\frac{L_1 + L_2}{L_1 L_2 C_f}}, \tag{33}$$

During the L_f sensitivity analysis, $L_f = L_1 + L_2$ and the ratio $L_1 : L_2 = 2 : 1$ is kept constant. The switching-level model also uses a 1.5 ohm series damping resistor and $C_{DC} = 5$ mF. C_f is held fixed because it is constrained primarily by reactive-power and resonance limits, whereas L_f is the investigated filter-design degree of freedom.

2.4. Input Factors, Uncertainty Model, and Operating Regime Segmentation

For the main ten-factor sensitivity experiment, the factor vector is:

$$z = \left[G,\ T_c,\ T_{\mathrm{amb}},\ V_g,\ \lambda,\ f_s,\ L_f,\ R_{\mathrm{th,eq}},\ ILR,\ k_{\mathrm{MPPT}}\right]^T \tag{34}$$

The grid frequency f_g is included in operating-profile construction and in grid-stress flagging, but it is not included in the main ten-factor sensitivity experiment because its variation is narrow in the benchmark. The filter capacitor C_f is also fixed for the reasons given in Section 2.3.

The ranges in Table 4 define the admissible stress-test domain rather than manufacturer tolerances alone. The annual baseline trajectory uses the dynamic T_c model in Equation (21), whereas the Sobol/Saltelli stress-test samples the retained factors independently within the distributions in Table 4. The resulting indices are therefore independent-input variance-based stress-test indices, not correlated-input Shapley effects. The local nominal value $\lambda_0 = 0.921$ is a high-output design point; the mean of Beta(2.8,1.9) mapped to [0.1,1.0] is approximately 0.64.

Table 4. Sensitivity factors, nominal values, uncertainty distributions, and rationale.

Factor	Nominal Value	Distribution/Range	Rationale
$\boldsymbol{G}$	850 W/m^2	Annual profile: empirical daylight [50, 1100] W/m^2; Sobol stress-test: U [50, 1100] W/m^2	Daylight domain excluding inactive night intervals
$\boldsymbol{T_c}$	55 °C	Annual profile: Equation (23); Sobol stress-test: $TN\left(45, 12^2;\ [15,\ 75]\right)$ °C	Separates profile generation from independent-input variance decomposition
$\boldsymbol{T_{\mathrm{amb}}}$	31 °C	$TN\left(26, 9^2;\ [0,\ 45]\right)$ °C	Representative annual ambient-temperature envelope
$\boldsymbol{V_g}$	400 V	$TN\left(400, 8^2;\ [360,\ 440]\right)$ V	±10% grid-voltage stress envelope
$\boldsymbol{\lambda}$	0.921	Beta(2.8,1.9) mapped to [0.1, 1.0]	High-output local point; mapped mean is approximately 0.64
$\boldsymbol{f_s}$	10 kHz	U [8, 12] kHz	Controller-tuning interval
$\boldsymbol{L_f}$	1.8 mH	U [1.6, 2.0] mH	Filter-design alternatives with $L_1 : L_2 = 2 : 1$
$\boldsymbol{R_{\mathrm{th,eq}}}$	33.5 K/kW	U [28, 39] K/kW	Equivalent thermal-path uncertainty
$\boldsymbol{ILR}$	1.20	U [1.10, 1.30]	Practical DC/AC sizing interval
$\boldsymbol{k_{\mathrm{MPPT}}}$	0.018	U [0.014, 0.022]	MPPT dynamic-gain interval

The scenario modifications are defined reproducibly as follows: baseline uses Table 4; high-temperature uses $T_{\mathrm{amb}} \sim TN\left(38, 4^2; [30,\ 45]\right)$ °C and $T_c \sim TN\left(65, 6^2; [50,\ 75]\right)$ °C; high-irradiance/clipping uses $G \sim U[850,\ 1100]$ W/m^2; and grid-stress uses a 50/50 mixture of $V_g \sim U[360,\ 380]$ V and $V_g \sim U[420,\ 440]$ V, with $f_g \sim U[49.7,\ 50.3]$ Hz used only for regime flagging. All other factors retain their baseline distributions.

The admissible operating domain is:

$$\mathcal{D} = \{(x, \theta, m) | 550 \le V_{DC} \le 950,\ I_{AC} \le I_{AC,\max},\ T_j \le 125\ ^\circ\mathrm{C},\ |Q_{AC}| \le Q_{\max},\ m \in \mathcal{M}\} \tag{35}$$

The mode segmentation rules used prior to regime-conditioned sensitivity analysis are summarized in Table 5.

Table 5. Mode segmentation rules used prior to regime-conditioned sensitivity analysis.

Operating Mode	Criterion
Thermal derating	$T_j \ge 105\ ^\circ$C and $P_{AC} < 0.98P_{\mathrm{rated}}$
Grid-stress	$\left|\frac{V_g}{V_{nom}} - 1\right| \ge 0.05$ or $|f_g - 50| \ge 0.2$ Hz; if voltage THD is available, $THD_V \ge 3\%$
Clipping	$P_{PV,\mathrm{av}} > P_{\mathrm{rated}}$ and $P_{AC} \ge 0.98P_{\mathrm{rated}}$
Nominal	$0.70P_{\mathrm{rated}} \le P_{AC} < 0.98P_{\mathrm{rated}}$, $G \ge 600$ W/m^2, $T_j < 105\ ^\circ$C and no grid-stress flag
Part-load	$0.10P_{\mathrm{rated}} \le P_{AC} < 0.70P_{\mathrm{rated}}$ without clipping, derating or grid-stress
Priority order	thermal derating $\to$ grid-stress $\to$ clipping $\to$ nominal $\to$ part-load

The minimum KPI package is $K_{\min} = \{E_{AC},\ \eta_{\mathrm{avg}},\ PF_{\mathrm{med}},\ THD_{I,\mathrm{med}},\ THD_{I,95},\ r_{VDC,\mathrm{med}},\ C_{\mathrm{clip}},\ HT_{\mathrm{med}},\ Availability,\ CF\}$.

2.5. Local, Morris and Sobol/Saltelli Sensitivity Analysis

The first level of the proposed framework involves local sensitivity analysis around a pre-selected representative operating point. The local normalized sensitivity for each KPI Y_j and each factor z_i is defined as

$$S_{i,j}^{loc}(z_0) = \left.\frac{\partial Y_j}{\partial z_i}\right|_{z_0} \frac{z_{i,0}}{Y_j(z_0)}, \tag{36}$$

where z_0 is the nominal factor vector.

When the analytical derivative is unavailable, a central finite difference with a 2% perturbation is used, and both perturbed states must remain in $\mathcal{D}$.

The second level is Morris screening. For each factor, the mean absolute elementary effect μ_i^* measures overall influence, while σ_i indicates nonlinearity and/or interaction-driven behavior. The Morris design uses eight levels and twenty random trajectories.

The third level is Sobol/Saltelli global sensitivity analysis. For a selected KPI $Y = f(z_1, \ldots, z_n)$, S_i measures the direct variance contribution and S_{Ti} includes all interaction terms involving factor i; $\Delta_i = S_{Ti} - S_i$ is used as an interaction indicator. After Morris screening, $D = 9$ factors are retained. With $N = 2048$ and $calc\_second\_order = True$, the Saltelli design requires $N(2D+2) = 40{,}960$ model evaluations per scenario. All KPIs are evaluated simultaneously in each model run. The random seed is 202601, and convergence is checked by comparing dominant S_{Ti} values at $N = 1024$ and $N = 2048$; changes below 0.02 are considered practically stable.

2.6. Cross-Check Procedure for the Reduced-Order Model

To verify that the reduced-order benchmark preserves the dominant converter trends, a switching-level reference model of the same two-level three-phase inverter is evaluated for nominal, clipping-prone, high-temperature, and grid-stress windows. The model uses SVPWM at $f_s = 10$ kHz, the LCL values in Table 3, the 20 Hz SRF-PLL, a 1 kHz inner dq-current loop, a 20 Hz outer DC-link loop and the $Q(V)$ law in Equations (25)–(29). The cross-check workflow is illustrated in Figure 4.

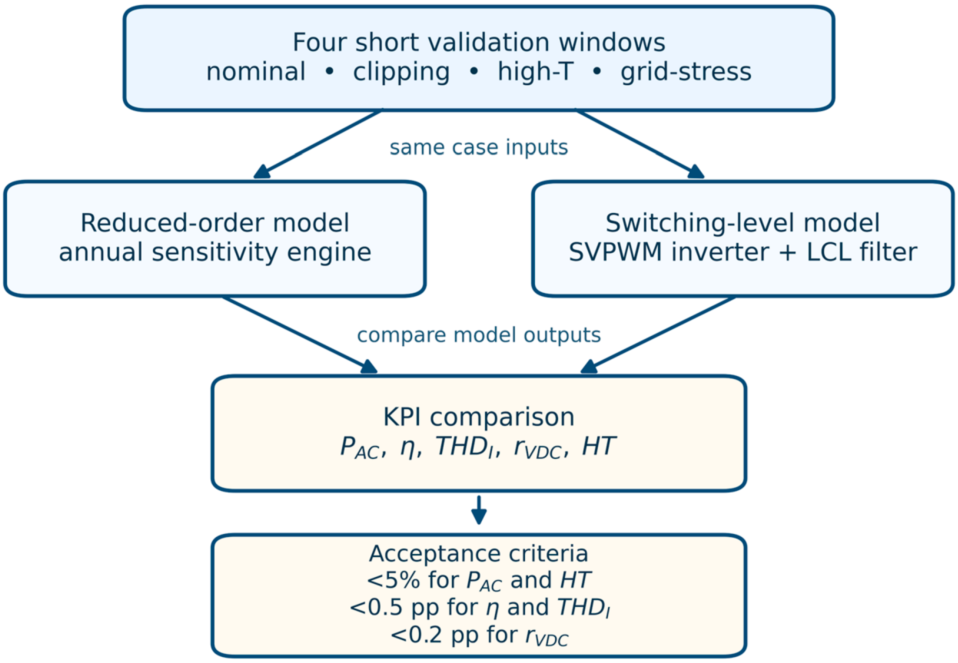

Figure 4. Cross-check protocol between the annual reduced-order benchmark and short-window switching-level simulation. Blue boxes denote the reduced-order and switching-level model paths, and pale boxes denote KPI comparison and acceptance criteria.

Each validation window is simulated for 2.0 s with a fixed integration time step of 1 microsecond. The first 0.5 s is excluded as a settling interval, and the reported KPIs are averaged over the remaining 1.5 s. The thermal state is initialized at the case-specific value listed in Table 6 because the 2 s electrical window is too short to reproduce the preceding thermal mission profile. The cross-check is not a substitute for full-year switching simulation or field validation.

Table 6. Short-window switching-level cross-check of the reduced-order benchmark.

Case	G [W/m^2]	T_{amb} [°C]	T_c [°C]	V_g [V]	P_{AC} RO/SW [kW]	η RO/SW [%]	THD_I RO/SW [%]	r_{VDC}/HT RO/SW [%]/[°C]
Nominal	850	31	55	400	92.1/91.2	98.0/97.8	2.6/2.8	1.6/1.7 31.0/30.1
Clipping-prone	1050	34	61	400	100.0/98.9	97.7/97.5	3.0/3.2	1.9/2.0 24.5/23.7
High-temperature	900	42	70	400	84.7/83.1	97.1/96.9	3.2/3.5	2.0/2.1 17.2/16.6
Grid-stress	850	31	55	370	90.8/89.4	97.6/97.3	4.8/5.1	2.4/2.5 28.8/27.9

The relative errors for P_{AC} and HT are calculated as:

$$\varepsilon_Y = \frac{|Y_{\mathrm{RO}} - Y_{\mathrm{SW}}|}{|Y_{\mathrm{SW}}|} \times 100\% \quad (37)$$

In Table 6, RO denotes the annual reduced-order model and SW denotes the switching-level reference result. The maximum deviations are 1.93% for P_{AC}, 0.30 percentage points for η, 0.30 percentage points for THD_I, 0.10 percentage points for r_{VDC} and 3.61% for HT. These deviations satisfy the adopted screening limits of 5% for P_{AC} and HT, 0.5 percentage points for eta and THD_I, and 0.2 percentage points for r_{VDC}.

2.7. Preprocessing, Software and Reproducibility Settings

Preprocessing includes synchronization to a common 1 min time base, interpolation for gaps up to 5 min, exclusion of longer gaps, removal of physically impossible values, event-flag handling, and exclusion of inactive night intervals from sensitivity evaluation. Supplementary File S1 contains the synthetic full-year profile, the 182,412-record active analysis subset, model coefficients, scenario definitions, validation-window data, processed KPI/sensitivity tables, executable Python functions, figure scripts, software requirements and a SHA-256 manifest.

3. Results

3.1. Basic Operating Profile and Reference Case

Table 7 contains the aggregated KPIs and regime shares, while Figure 5 shows the time-domain behavior that motivates the subsequent regime-conditioned sensitivity analysis. Nominal and part-load operation dominate, but clipping, derating, and grid-stress intervals remain sufficiently represented to activate different physical constraints.

Table 7. Baseline KPIs and regime distributions for the representative benchmark year.

Indicator	Designation	Value
AC energy	E_{AC}	165.4 MWh/year
Energy-averaged efficiency	η_{avg}	97.82%
Availability	$Availability$	98.9%
Capacity factor	CF	18.9%
Median current power factor	$PF_{I,\text{med}}$	0.992
PF interquartile range	PF_{IQR}	0.985–0.998
Median harmonic distortion	THD_{med}	2.84%
95th percentile current ***THD***	$THD_{I,95}$	4.12%
Median DC bus ripple	$r_{V_{DC},\text{med}}$	1.87%
Median thermal headroom	HT_{med}	28.6 °C
Clipping index	C_{clip}	4.7%
Nominal active-time share	m_{nom}	55.2%
Part-load share	m_{part}	29.7%
Clipping share	m_{clip}	9.1%
Thermal derating share	m_{der}	3.0%
Grid-stress share	m_{grid}	3.0%

Figure 5a shows that T_c follows irradiance with thermal delay rather than instantaneously. In Figure 5b, P_{AC} follows $P_{PV,\text{av}}$ outside clipping and derating, while the rated limit makes clipping explicit. Figure 5c masks inactive and very-low-power intervals. Figure 5d reports THD_I, not voltage THD. The selected components in Figure 5e are 0.55% (3rd), 1.55% (5th), 1.15% (7th), 0.70% (11th) and 0.50% (13th) of the fundamental; the 5th harmonic is the largest, followed by the 7th. The remaining harmonic orders account for the difference between this selected spectrum and complete THD_I.

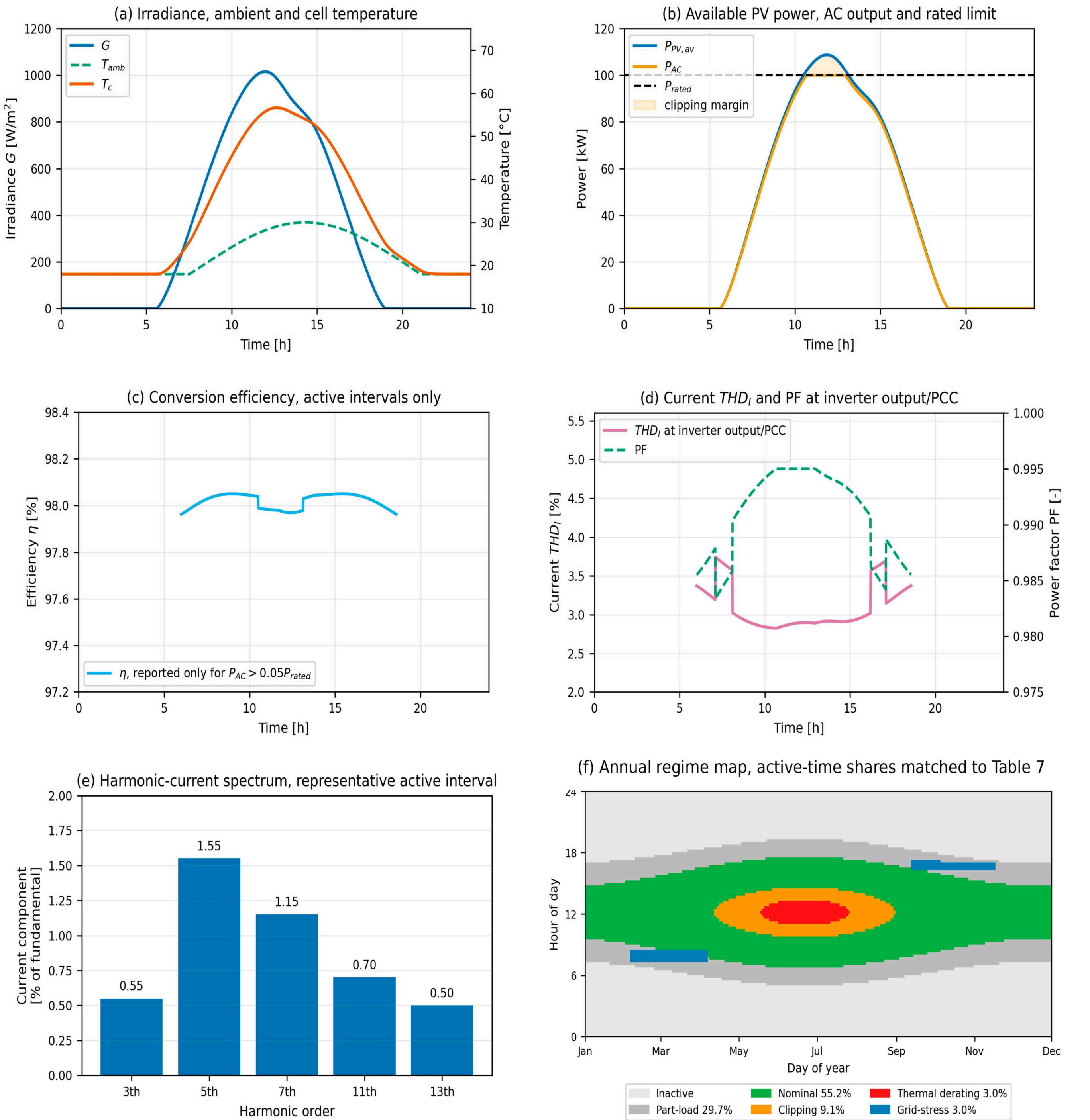

Figure 5. Baseline operating behavior of the 100 kW PV inverter benchmark. Panel (**a**) shows G, T_{amb} and T_c with thermal inertia; panel (**b**) compares $P_{PV,\text{av}}$, P_{AC} and P_{rated}; panel (**c**) reports η only for $P_{AC} > 0.05P_{\text{rated}}$; panel (**d**) reports current THD_I and PF at the inverter output/PCC; panel (**e**) gives the representative harmonic-current spectrum; and panel (**f**) gives the annual regime map with active-time shares matched to Table 7.

3.2. Local Sensitivity Analysis Around the Nominal Operating Point

The local sensitivity analysis is conducted around the nominal operating point.

$$z_0 = [850, 55, 31, 400, 0.92, 10, 1.8, 33.5, 1.20, 0.018] \tag{38}$$

with components corresponding to G, T_c, T_{amb}, V_g, λ, f_s, L_f, $R_{\text{th,eq}}$, ILR and k_{MPPT}. Grid frequency is fixed for this experiment and is therefore not included in z_0.

Figure 6 and Table 8 should be interpreted together. Increasing f_s improves harmonic performance but increases switching losses, which creates a local $\eta - THD_I$ trade-off. Local analysis is therefore useful for controller tuning but cannot replace the regime-aware global analysis of clipping, derating and grid-stress interactions.

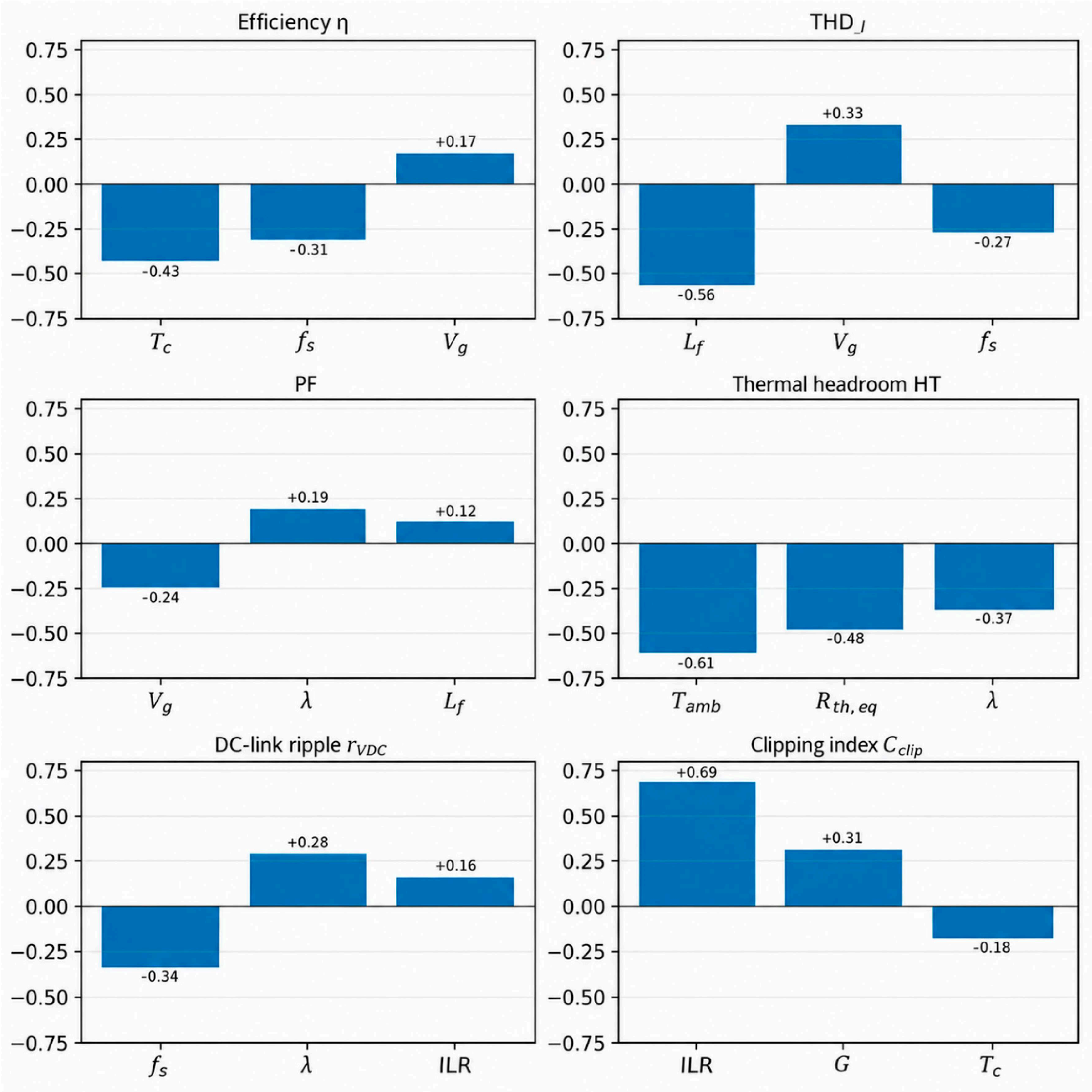

Figure 6. Local normalized sensitivities. Positive values indicate that the KPI increases with the factor, and negative values indicate that it decreases; Table 8 gives the numerical values.

Table 8. Local normalized sensitivities around the corrected nominal operating point.

KPI	Factor 1	S^{loc}	Factor 2	S^{loc}	Factor 3	S^{loc}	Brief Engineering Interpretation
$\boldsymbol{\eta}$	T_c	−0.43	f_s	−0.31	V_g	+0.17	Temperature and switching loss dominated local efficiency behavior
$\boldsymbol{THD_I}$	L_f	−0.56	V_g	+0.33	f_s	−0.27	Power-quality sensitivity to filtering and voltage and switching frequency
$\boldsymbol{PF}$	V_g	−0.24	λ	+0.19	L_f	+0.12	PF depends strongly on grid-side operating point and reactive-power model

Table 8. *Cont.*

KPI	Factor 1	S^{loc}	Factor 2	S^{loc}	Factor 3	S^{loc}	Brief Engineering Interpretation
HT	T_{amb}	−0.61	R_{th}	−0.48	λ	−0.37	Thermal reserve is determined by ambient loading and equivalent thermal path
r_{VDC}	f_s	−0.34	λ	+0.28	ILR	+0.16	DC-link ripple sensitivity to switching and loading
C_{clip}	ILR	+0.69	G	+0.31	T_c	−0.18	Clipping is dominated by oversizing and irradiance

3.3. Morris Screening and Factors Selection

Morris screening is used to distinguish regular high-influence factors from factors whose effects are nonlinear or interaction-dependent. Factors with high μ^* and low σ, such as T_c for efficiency, behave relatively regularly across the sampled domain. In contrast, V_g, G and λ show larger σ values, indicating that their influence depends on the active operating regime. This is the reason for retaining them for Sobol/Saltelli analysis even when their first-order local influence is not always dominant. The screening statistics are reported in Table 9.

Table 9. Morris screening statistics for the main KPIs.

KPI	Factor	μ^*	σ
η	T_c	0.41	0.07
η	f_s	0.33	0.06
η	V_g	0.19	0.12
η	λ	0.16	0.09
THD	L_f	0.48	0.10
THD	V_g	0.35	0.19
THD	f_s	0.29	0.14
THD	λ	0.20	0.17
PF	V_g	0.27	0.15
PF	λ	0.23	0.08
PF	L_f	0.15	0.10
HT	T_{amb}	0.53	0.09
HT	$R_{\text{th,eq}}$	0.47	0.07
HT	λ	0.38	0.14
HT	T_c	0.21	0.16
C_{clip}	ILR	0.62	0.11
C_{clip}	G	0.46	0.22
C_{clip}	T_c	0.24	0.18

The factors retained for Sobol/Saltelli analysis are $\{G, T_c, T_{\text{amb}}, V_g, \lambda, f_s, L_f, R_{\text{th,eq}}, ILR\}$. The MPPT parameter k_{MPPT} is excluded from the main global stage because μ^* remains below 0.10 for the primary quasi-steady KPIs. This does not imply that MPPT dynamics are irrelevant for transient studies. It only reflects the focus of the present benchmark on operating-profile KPIs. The corresponding Morris $\mu^* - \sigma$ diagrams are shown in Figure 7.

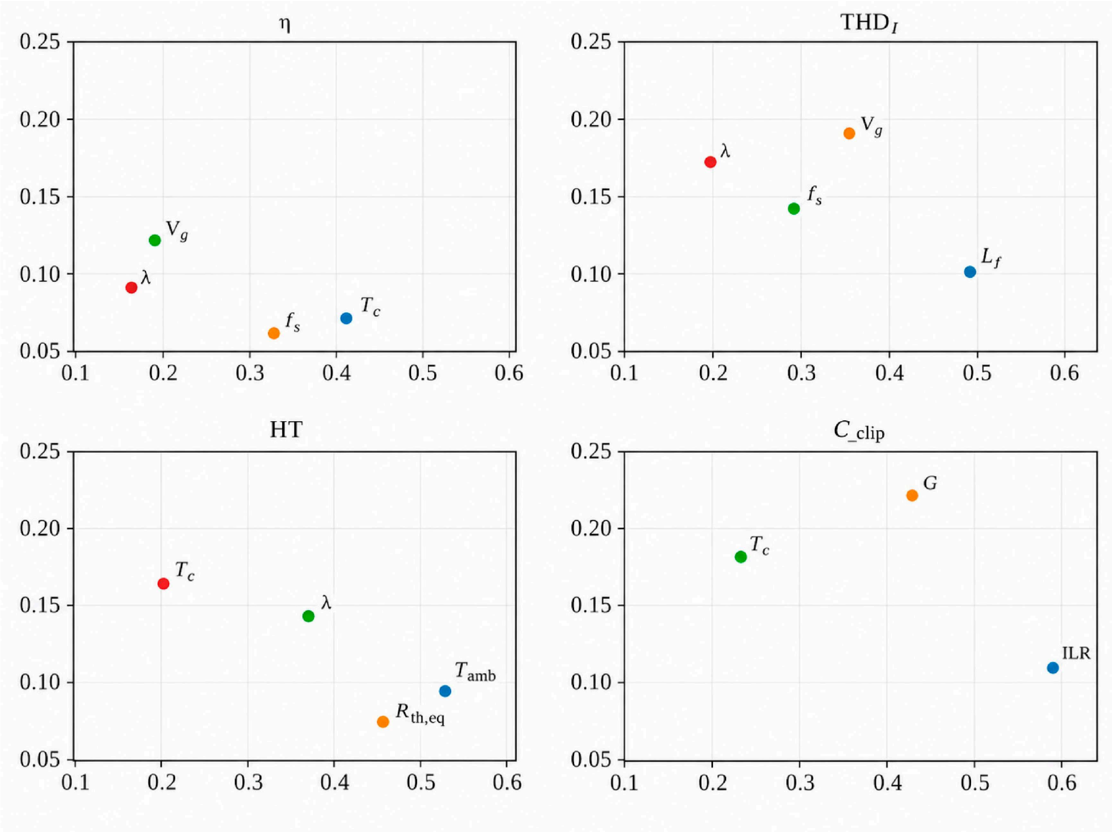

Figure 7. Morris $\mu^* - \sigma$ diagrams. High μ^* indicates strong overall influence, whereas high σ indicates nonlinear or interaction-dependent behavior. Each colored dot represents one retained factor labelled by its symbol.

3.4. Sobol/Saltelli Global Sensitivity Analysis

The gap between S_{Ti} and S_i is especially important for V_g in THD_I and PF, and for G and ILR in C_{clip}. These gaps indicate that the corresponding factors do not act only through direct variance contributions, but also through regime-dependent interactions. This explains why the ranking obtained from local sensitivity around the nominal point differs from the global ranking under uncertainty. Table 10 reports the corresponding first-order, total-effect and interaction-gap values.

Table 10. Sobol/Saltelli first-order and total-effect indices, including the T_c rows for HT and C_{clip}.

KPI	Factor	S_i	S_{T_i}	Δ_i=$S_{T_i}-S_i$
η	T_c	0.28	0.36	0.08
η	f_s	0.17	0.24	0.07
η	V_g	0.11	0.20	0.09
η	λ	0.08	0.15	0.07
THD	L_f	0.24	0.34	0.10
THD	V_g	0.18	0.31	0.13
THD	f_s	0.14	0.22	0.08
PF	V_g	0.21	0.33	0.12
PF	λ	0.16	0.22	0.06
PF	L_f	0.09	0.17	0.08

Table 10. *Cont.*

KPI	Factor	S_i	S_{T_i}	$\Delta_i = S_{T_i} - S_i$
HT	T_{amb}	0.31	0.41	0.10
HT	$R_{\mathrm{th,eq}}$	0.24	0.34	0.10
HT	λ	0.12	0.23	0.11
HT	T_c	0.09	0.17	0.08
$\boldsymbol{C_{\mathrm{clip}}}$	ILR	0.37	0.52	0.15
$\boldsymbol{C_{\mathrm{clip}}}$	G	0.22	0.39	0.17
$\boldsymbol{C_{\mathrm{clip}}}$	T_c	0.10	0.21	0.11
$\boldsymbol{r_{VDC}}$	f_s	0.19	0.28	0.09
$\boldsymbol{r_{VDC}}$	λ	0.14	0.24	0.10
$\boldsymbol{r_{VDC}}$	V_g	0.09	0.18	0.09

The largest pairwise contributions are listed in Table 11.

Table 11. Most significant pairwise interactions.

KPI/Scenario	Interaction Pair	Second-Order Contribution
$\boldsymbol{THD_I}$**, grid-stress**	$V_g \times L_f$	0.12
$\boldsymbol{C_{\mathrm{clip}}}$**, high-irradiance**	$ILR \times G$	0.11
***HT*, high-temperature**	$T_{\mathrm{amb}} \times R_{\mathrm{th,eq}}$	0.07
$\boldsymbol{\eta}$**, baseline**	$T_c \times f_s$	0.05

Figure 8 summarizes the global sensitivity indices and scenario-dependent rank shifts.

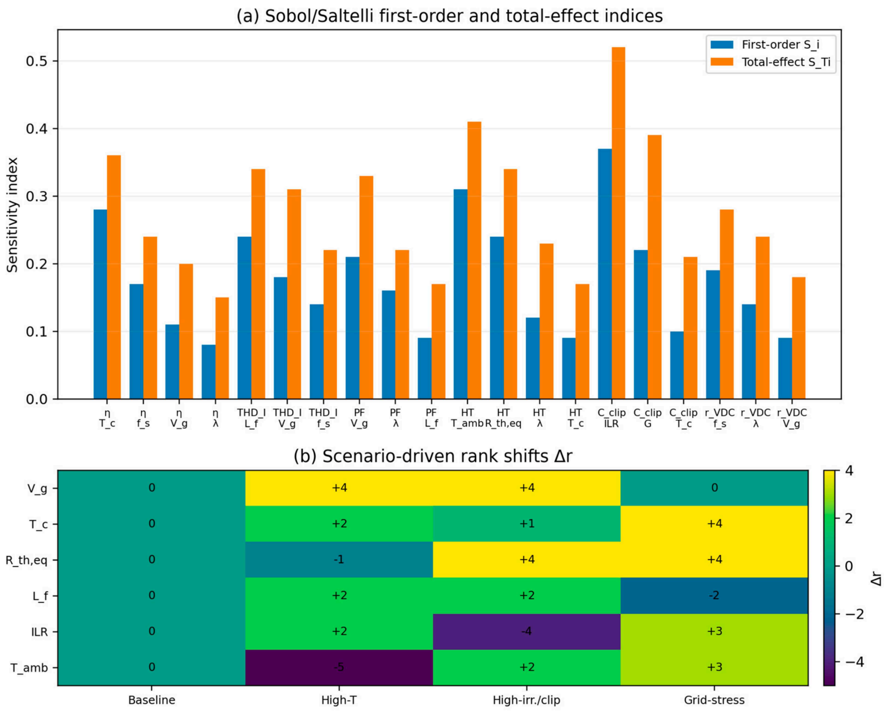

Figure 8. Global sensitivity results and scenario-dependent rank shifts. Panel (**a**) shows first-order and total-effect Sobol/Saltelli indices; panel (**b**) shows changes in factor rank between scenarios.

3.5. Scenario-Dependent Inverter Outputs and Factor Importance

To avoid reporting sensitivity rankings without corresponding inverter outputs, Table 12 gives the main KPI values for each scenario before the dominant factors are interpreted. The table complements Figure 5 with case-specific high-temperature, clipping-prone and grid-stress outputs.

Table 12. Scenario-specific inverter outputs and dominant total-effect factors.

Scenario	E_{AC}	η_{avg}	$P_{AC,95}$	PF_{med}	$THD_{I,med}$	$THD_{I,95}$	$r_{VDC,med}$	HT_{med}	C_{clip}	Dominant Total-Effect Factors
Baseline	165.4 MWh	97.82%	97.6 kW	0.992	2.84%	4.12%	1.87%	28.6 °C	4.7%	V_g, T_c, $R_{th,eq}$, L_f, ILR
High-temperature	158.9 MWh	97.18%	93.4 kW	0.990	3.05%	4.58%	2.05%	17.2 °C	3.1%	T_{amb}: 0.53; $R_{th,eq}$: 0.42; λ: 0.27
High-irradiance/clipping	174.8 MWh	97.65%	100.0 kW	0.991	2.95%	4.36%	2.12%	24.1 °C	11.8%	ILR: 0.64; G: 0.45; T_c: 0.24
Grid-stress	163.2 MWh	97.54%	95.8 kW	0.983	3.63%	5.46%	2.34%	27.4 °C	4.9%	THD_I: V_g: 0.47, L_f: 0.38, f_s: 0.25; PF: V_g: 0.44, λ: 0.24

The high-temperature scenario reduces annual AC energy and thermal headroom because derating becomes more frequent. The high-irradiance/clipping scenario increases annual energy but raises C_{clip} to 11.8%, showing that part of the additional DC power is limited by the AC rating. Under grid-stress, THD_I, $THD_{I,95}$ and r_{VDC} increase while PF decreases, shifting factor importance toward V_g, L_f and f_s. Figure 9 visualizes these relative KPI changes.

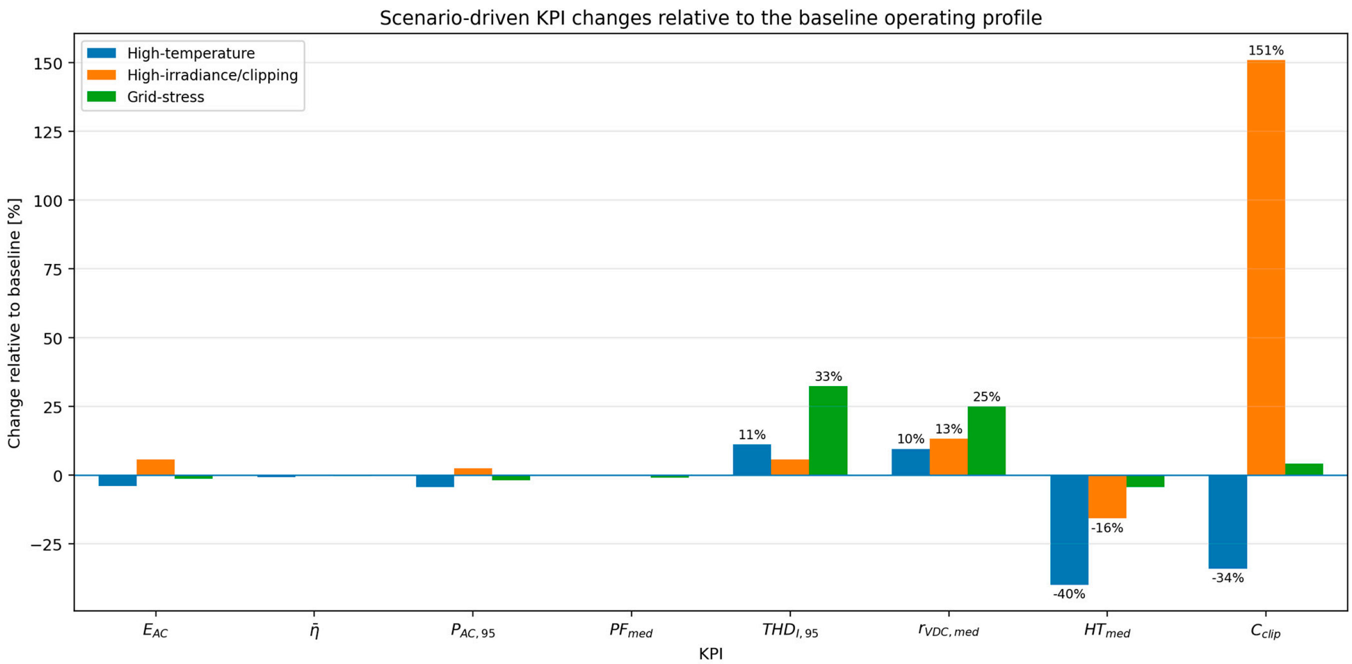

Figure 9. Scenario-driven KPI changes relative to the baseline operating profile. Bar colors correspond to the high-temperature, high-irradiance/clipping and grid-stress scenarios indicated in the legend.

Positive bars indicate an increase relative to the baseline and negative bars indicate a decrease. The figure highlights the thermal/energy penalty of the high-temperature case, the large clipping increase under high irradiance and the power-quality deterioration under grid-stress.

https://doi.org/10.3390/pr14162677

3.6. Composite Uncertainty-Aware Factor Prioritization

The final ranking is an engineering prioritization for the selected benchmark and uncertainty model. Because local, Morris and Sobol quantities have different numerical scales, each component q_i is min-max normalized across retained factors before aggregation:

$$q_{\text{tilde}_i} = \frac{[q_i - \min_k(q_k)]}{[\max_k(q_k) - \min_k(q_k)]} \tag{39}$$

A composite importance score is calculated to obtain a single engineering ranking of the factors, which combines local sensitivity, Morris screening, and total-effect global sensitivity:

$$R_i = 0.30 \ \text{mean}_j\left(\left|S_{i,j}^{loc}\right|\right)_{\text{tilde}} + 0.25 \ \text{mean}_j\left(\mu_{i,j}^*\right)_{\text{tilde}} + 0.45 \ \text{mean}_j\left(S_{Ti,j}\right)_{\text{tilde}} \tag{40}$$

where $\text{mean}_j\left(\left|S_{i,j}^{loc}\right|\right)_{\text{tilde}}$ is the average absolute local sensitivity of the factor, $\text{mean}_j\left(\mu_{i,j}^*\right)_{\text{tilde}}$ is the average Morris influence measure, and $\text{mean}_j\left(S_{Ti,j}\right)_{\text{tilde}}$ is the average total-effect contribution across KPIs and scenarios.

The larger weight assigned to the total-effect term reflects the uncertainty-aware objective of the composite ranking. The scores in Table 13 use this normalization.

Table 13. Final uncertainty-aware ranking of factors.

Final Rank	Factor	Composite Score R_i	Practical Interpretation
1	V_g	0.348	Critical for power quality, *PF* and grid-stress robustness
2	T_c	0.332	Dominant for efficiency behavior and thermal coupling
3	$R_{\text{th,eq}}$	0.301	Key for thermal reserve and derating propensity
4	L_f	0.287	Main design lever for THD_I and filtering performance
5	ILR	0.273	Critical for clipping behavior and oversizing trade-offs
6	T_{amb}	0.268	Important for thermal stress and seasonal variability
7	f_s	0.261	Suitable for local control tuning and alarm logic
8	λ	0.248	Related to operating point dependence and ripple behavior
9	G	0.236	Important mainly in clipping-prone and energy-driven scenarios
10	k_{MPPT}	0.072	Low overall impact in the present quasi-steady benchmark

V_g, T_c and $R_{\text{th,eq}}$ rank highest because they affect multiple KPIs and participate in regime-dependent interactions. In contrast, k_{MPPT} remains low in the considered benchmark because the analysis focuses on quasi-steady operating profiles rather than fast MPPT transients.

3.7. Comparison with Field and Literature Evidence

The synthetic benchmark is interpreted against measured and standardized evidence rather than presented as field validation. Alawasa and Al-Badi [37] report location- and equipment-dependent power-quality behavior in an academic distribution system. Atsu et al. [38] show that outdoor current THD and PF behavior can differ substantially from steady PV-simulator results, while voltage THD may remain within limits. IEC 61683 [39] provides the standardized context for power-conditioner efficiency measurement. These sources support separate reporting of THD_I and THD_V and regime-specific interpretation of PF, efficiency and thermal behavior. Table 14 compares the benchmark outputs with this field and literature evidence.

Table 14. Comparison of benchmark outputs with field and literature evidence.

Indicator	Present Benchmark	Field/Literature Comparison	Interpretation
η_{avg}	97.82% baseline; 97.18% high-temperature	IEC 61683 defines standardized power-conditioner efficiency measurement procedures [39].	The benchmark is consistent with high-efficiency operation, but is not a substitute for laboratory certification.
PF_{med}	0.992 baseline; 0.983 grid-stress	Outdoor microinverter results show that PF varies with irradiance and real operating conditions [38].	Supports regime-aware PF reporting rather than one pooled annual value.
$THD_{I,\mathrm{med}}$	2.84% baseline; 3.63% grid-stress	Measured distribution-system power-quality results show location- and equipment-dependent harmonic behavior [37].	Supports comparison of simulated THD_I with measured PCC/inverter-output evidence.
$THD_{I,95}$	4.12% baseline; 5.46% grid-stress	Outdoor current THD can exceed steady PV-simulator values while voltage THD remains within limits [38].	Supports explicit separation of THD_I and THD_V.
HT_{med}	28.6 °C baseline; 17.2 °C high-temperature	Mission-profile and inverter-diagnostics studies link hot-spot loading and cooling-path condition to reliability [22,23].	Supports reporting thermal headroom as a separate KPI.
C_{clip}	4.7% baseline; 11.8% clipping scenario	Sizing-ratio and clipping studies show that ILR and irradiance alter energy-yield and loss signatures [20,26].	Supports the $ILR \times G$ interaction in clipping-prone operation.

4. Discussion

4.1. Added Value of the Hierarchical Framework

The added value of the proposed framework is not the isolated observation that operating point, filtering, and grid voltage affect efficiency, PF, or THD, which is already known from converter theory. The added value is that the framework quantifies how the relative importance of these factors changes across operating regimes and uncertainty scenarios, and separates direct effects from interaction-driven effects. This enables different engineering decisions: local indices support setpoint tuning, Morris indices identify factors requiring global analysis, and Sobol/Saltelli total-effect indices reveal regime-dependent robustness drivers that would be hidden in a pooled annual ranking.

Local sensitivity provides the sign and local strength of influence near the design point. Morris screening expands the investigation to a wider input domain and identifies factors whose effects are nonlinear or interaction-prone. Sobol/Saltelli analysis then quantifies direct and total variance contributions, allowing grid-stress, thermal, and clipping effects to be interpreted as regime-dependent robustness issues rather than as isolated nominal sensitivities.

4.2. Implications for Design, Control Tuning and Monitoring

From a design perspective, the results show that $R_{\mathrm{th,eq}}$, L_f and ILR should not be optimized only for nominal performance. $R_{\mathrm{th,eq}}$ affects thermal headroom and derating risk; L_f governs harmonic attenuation and PF behavior under grid-stress conditions; and ILR controls the trade-off between annual energy capture and clipping losses. From a control-tuning perspective, f_s illustrates a direct efficiency-power-quality compromise:

increasing f_s reduces THD_I and r_{VDC} but increases switching losses. From a monitoring perspective, the dominant global factors V_g, T_c and $R_{\mathrm{th,eq}}$ should be tracked as part of trend-based diagnostics rather than only through fixed threshold alarms.

It is particularly important from the perspective of monitoring systems to conclude that factors should not be prioritized solely according to the absolute value of a given sensitivity index, but according to the combination of sensitivity and the frequency of the mode in which it is relevant. A mode-dependent alarm significance index for this purpose can be introduced

$$A_{i,j}^{(m)} = p_m \left| S_{i,j}^{loc,(m)} \right|, \tag{41}$$

where p_m is the probability of occurrence of regime m, and $S_{i,j}^{loc,(m)}$ is the local sensitivity of KPI j to factor i in that regime. Thus, a factor that has a very high local influence but occurs in a rare regime can be evaluated differently from a factor with moderate sensitivity but a high frequency of occurrence in real operation.

4.3. Predictive Maintenance and Risk-Informed Prioritization

In predictive maintenance, coordinated changes in η, THD_I, r_{VDC} and HT must be distinguished from normal climate-induced variability. An increasing sensitivity of HT to T_{amb} and $R_{\mathrm{th,eq}}$ may indicate loss of thermal reserve, poor cooling or a degraded thermal path. Similarly, increasing sensitivity of THD_I and r_{VDC} to V_g, L_f or f_s can indicate reduced harmonic robustness, filter degradation, DC-link aging or control deterioration. The maintenance priority score can therefore combine factor importance, exposure to KPI-limit violations and degradation susceptibility:

$$M_i = \alpha R_i + \beta P_i^{exc} + \gamma D_i, \;\; \alpha + \beta + \gamma = 1, \tag{42}$$

where R_i is the composite sensitivity score from (40), P_i^{exc} is the probability that the KPI associated with the factor will exceed a specified operating limit, and D_i is an indicator of susceptibility to degradation. Thus, a factor that is both sensitivity-dominant—often associated with limit violations—and physically susceptible to degradation processes will receive a higher maintenance priority.

4.4. Study Limitations

The main limitation is that the benchmark remains synthetic. The reduced-order model is now explicitly specified and cross-checked in representative switching-level windows, but the annual sensitivity rankings are still conditional on the selected model, distributions, and segmentation thresholds. They should therefore be interpreted as a reproducible methodological demonstration, not as universal numerical rankings for all PV converters. Transferability to other topologies, cooling designs, grid codes and climates requires additional field validation. The composite ranking weights are also user-defined and should be re-evaluated for specific engineering objectives. Table 15 summarizes the corresponding mitigation strategies.

Table 15. Main limitations and mitigation strategies.

Limitation	Potential Impact	Strategy
Synthetic benchmark	Limited direct industrial transferability	Validation on multi-site field datasets
Conditional uncertainty model	Rankings depend on distributions and dependence structure	Use empirical sampling and scenario enrichment
Threshold regime segmentation	Mode boundaries can affect rankings	Perform sensitivity analysis of the segmentation thresholds

https://doi.org/10.3390/pr14162677

Table 15. *Cont.*

Limitation	Potential Impact	Strategy
Computational burden of global indices	Limits online deployment	Use surrogate models and adaptive sampling
Topology dependence	Dominant factors may shift for other converters	Perform cross-topology benchmark studies

4.5. Benchmark-Ready Reporting Recommendations

A sensitivity study becomes reproducible only if the operating domain, KPI definitions, uncertainty assumptions, preprocessing rules, segmentation thresholds, model coefficients, random seeds, and software settings are reported together with the numerical rankings. The proposed reporting package is:

$$B = \{K_{\min}, \mathcal{D}, \mathcal{M}, \Pi, \mathcal{U}, \mathcal{S}\}, \tag{43}$$

where $K_{\min}$ is the minimum KPI package, $\mathcal{D}$ is the admissible domain, $\boldsymbol{\mathcal{M}}$ is the regime logic, Π is provenance information, $\mathcal{U}$ is the uncertainty model and $\mathcal{S}$ is the software/code descriptor. Table 16 provides the recommended reporting checklist.

Table 16. Recommended benchmark-ready reporting checklist for PV converter sensitivity studies.

Reporting Item	Required Content
Converter description	Topology, nominal power, DC/AC ratio, basic parameters, control architecture
Operating domain	Voltage, current, temperature, reactive power and protection limits
Reduced-order model	Equations, coefficients, calibration points and validity limits
Validation	Representative switching-level or field comparison windows
KPI definitions	Formulas, aggregation windows and percentile indicators
Nominal point	Reference point and perturbation size for local sensitivity
Morris design	Number of levels, trajectories and selection criterion
Sobol/Saltelli settings	Retained factors, sample size and convergence check
Uncertainty model	Distributions, bounds, dependence structure and scenarios
Regime segmentation	Thresholds, priority order and event handling
Preprocessing	Resampling, missing data treatment, outlier policy and filtering
Software and code	Software versions, random seed and code availability
Data availability	Input profiles, model coefficients, KPI tables and access mode

5. Conclusions

This paper developed a regime-aware hierarchical framework for sensitivity analysis of PV converter operating profiles under climatic and grid uncertainty. The framework combines local normalized sensitivity indices, Morris screening and Sobol/Saltelli variance-based analysis in a single workflow. The purpose of this hierarchy is not to replace detailed converter simulation, but to provide a reproducible way to identify which factors dominate different KPIs and how their importance changes across operating regimes.

The 100 kW synthetic benchmark shows that factor importance is KPI- and regime-dependent. Local analysis is useful for nominal controller tuning and reveals direct trade-offs such as the efficiency–THD compromise associated with switching frequency. Morris screening identifies nonlinear or interaction-prone factors, while Sobol/Saltelli analysis shows that grid voltage, cell temperature, and equivalent thermal resistance dominate the global uncertainty-aware ranking in the considered benchmark. The strongest observed second-order contribution is associated with the interaction between grid voltage and filter inductance under grid-stress conditions.

The results confirm that pooled annual rankings can be misleading when clipping, thermal derating and grid-stress intervals are mixed with nominal operation. For this reason, sensitivity results should be reported conditionally by operating regime and accompanied by explicit uncertainty assumptions, segmentation rules, KPI definitions, and software settings.

The main limitation is that the benchmark is synthetic and depends on the selected reduced-order model and uncertainty distributions. Future work should validate the workflow on field datasets, extend it to other converter topologies, and combine it with surrogate models for faster digital-twin and predictive-maintenance applications.

Supplementary Materials: The following supporting information can be downloaded at: https://www.mdpi.com/article/10.3390/pr14162677/s1, File S1: Synthetic benchmark data and reproducibility package, including the full-year input profile, active analysis subset, reduced-order model coefficients, scenario definitions, preprocessing/profile-generation scripts, switching-reference settings, validation-window data, processed KPI and sensitivity tables, figure-generation scripts, software requirements, random seed and SHA-256 manifest.

Author Contributions: I.H., S.B. and M.K.V. were involved in the full process of producing this paper, including conceptualization, methodology, modeling, validation, visualization, and preparing the manuscript preparation. All authors have read and agreed to the published version of the manuscript.

Funding: The article processing charge (APC) was funded by Technical University of Sofia under its institutional agreement with MDPI, with financial support from the European Regional Development Fund within the Operational Programme "Bulgarian national recovery and resilience plan", procedure for direct provision of grants "Establishing of a network of research higher education institutions in Bulgaria", under Project BG-RRP-2.004-0005 "Improving the research capacity and quality to achieve international recognition and resilience of TU-Sofia (IDEAS)".

Data Availability Statement: The original contributions presented in this study are included in the article and Supplementary File S1. Supplementary File S1 contains the synthetic full-year input profile, the 182,412-record active analysis subset, reduced-order model coefficients, scenario definitions, preprocessing and profile-generation scripts, switching-reference settings, validation-window data, random seed, processed KPI and sensitivity tables, figure-generation scripts, software requirements and a SHA-256 manifest. Further inquiries can be directed to the corresponding author.

Acknowledgments: This work has been accomplished with financial support by the European Regional Development Fund within the Operational Programme "Bulgarian national recovery and resilience plan", procedure for direct provision of grants "Establishing of a network of research higher education institutions in Bulgaria", and under Project BG-RRP-2.004-0005 "Improving the research capacity and quality to achieve intErnAtional recognition and reSilience of TU-Sofia (IDEAS)".

Conflicts of Interest: The authors declare no conflicts of interest.

References

1. Teodorescu, R.; Liserre, M.; Rodríguez, P. *Grid Converters for Photovoltaic and Wind Power Systems*; Wiley: Chichester, UK, 2011. [CrossRef]
2. Villalva, M.G.; Gazoli, J.R.; Ruppert Filho, E. Comprehensive approach to modeling and simulation of photovoltaic arrays. *IEEE Trans. Power Electron.* **2009**, *24*, 1198–1208. [CrossRef]
3. De Soto, W.; Klein, S.A.; Beckman, W.A. Improvement and validation of a model for photovoltaic array performance. *Sol. Energy* **2006**, *80*, 78–88. [CrossRef]
4. Skoplaki, E.; Palyvos, J.A. On the temperature dependence of photovoltaic module electrical performance: A review of efficiency/power correlations. *Sol. Energy* **2009**, *83*, 614–624. [CrossRef]
5. Liserre, M.; Blaabjerg, F.; Hansen, S. Design and control of an LCL-filter-based three-phase active rectifier. *IEEE Trans. Ind. Appl.* **2005**, *41*, 1281–1291. [CrossRef]

6. Morris, M.D. Factorial sampling plans for preliminary computational experiments. *Technometrics* **1991**, *33*, 161–174. [CrossRef]
7. Campolongo, F.; Cariboni, J.; Saltelli, A. An effective screening design for sensitivity analysis of large models. *Environ. Model. Softw.* **2007**, *22*, 1509–1518. [CrossRef]
8. Sobol, I.M. Global sensitivity indices for nonlinear mathematical models and their Monte Carlo estimates. *Math. Comput. Simul.* **2001**, *55*, 271–280. [CrossRef]
9. Saltelli, A.; Annoni, P.; Azzini, I.; Campolongo, F.; Ratto, M.; Tarantola, S. Variance-based sensitivity analysis of model output: Design and estimator for the total sensitivity index. *Comput. Phys. Commun.* **2010**, *181*, 259–270. [CrossRef]
10. Saltelli, A.; Ratto, M.; Andres, T.; Campolongo, F.; Cariboni, J.; Gatelli, D.; Saisana, M.; Tarantola, S. *Global Sensitivity Analysis: The Primer*; Wiley: Chichester, UK, 2008. [CrossRef]
11. Pianosi, F.; Beven, K.; Freer, J.; Hall, J.W.; Rougier, J.; Stephenson, D.B.; Wagener, T. Sensitivity analysis of environmental models: A systematic review with practical workflow. *Environ. Model. Softw.* **2016**, *79*, 214–232. [CrossRef]
12. *IEEE Std 519-2022*; IEEE Standard for Harmonic Control in Electric Power Systems. IEEE: New York, NY, USA, 2022. [CrossRef]
13. *IEC 61724-1:2021*; Photovoltaic System Performance—Part 1: Monitoring. International Electrotechnical Commission: Geneva, Switzerland, 2021.
14. Herman, J.; Usher, W. SALib: An open-source Python library for sensitivity analysis. *J. Open Source Softw.* **2017**, *2*, 97. [CrossRef]
15. Morey, M.; Gupta, N.; Garg, M.M.; Kumar, A. A comprehensive review of grid-connected solar photovoltaic system: Architecture, control, and ancillary services. *Renew. Energy Focus* **2023**, *45*, 307–330. [CrossRef]
16. Abdulla, H.; Sleptchenko, A.; Nayfeh, A. Photovoltaic systems operation and maintenance: A review and future directions. *Renew. Sustain. Energy Rev.* **2024**, *195*, 114342. [CrossRef]
17. Bamisile, O.; Acen, C.; Cai, D.; Huang, Q.; Staffell, I. The environmental factors affecting solar photovoltaic output. *Renew. Sustain. Energy Rev.* **2025**, *208*, 115073. [CrossRef]
18. Hossain, M.K.; Chowdhury, P.; Nowshin, I.; Islam, M.R.; Al-Hysam, A.; Farrok, O. Grid-connected inverter for photovoltaic energy harvesting: Advances in topologies and control techniques. *Energy Convers. Manag. X* **2026**, *29*, 101422. [CrossRef]
19. Saedabad, Z.E.; Vahidi, B.; Jalilian, M.J. Harmonic stability of weak grid-connected solar power plant. *Electr. Power Syst. Res.* **2024**, *233*, 110471. [CrossRef]
20. Brito, E.M.S.; Cupertino, A.F.; Pereira, H.A.; Mendes, V.F. Reliability-based trade-off analysis of reactive power capability in PV inverters under different sizing ratio. *Int. J. Electr. Power Energy Syst.* **2022**, *136*, 107677. [CrossRef]
21. Chai, Q.; Zhang, C.; Dong, Z.Y.; Xu, Y. Operational reliability assessment of photovoltaic inverters considering voltage/VAR control function. *Electr. Power Syst. Res.* **2021**, *190*, 106706. [CrossRef]
22. Ryu, T.; Choi, U.-M.; Vernica, I.; Blaabjerg, F. Effect of thermal loading definitions on the mission profile-based reliability evaluation of power devices in PV inverters. *Microelectron. Reliab.* **2022**, *138*, 114650. [CrossRef]
23. Song, Q.; Ma, M.; Guo, W.; Jiang, T.; Pan, N. Health state diagnosis of air duct for photovoltaic inverter based on PSO-SVM classifier. *Microelectron. Reliab.* **2023**, *150*, 115084. [CrossRef]
24. Zhang, F.; Wang, X.; Wang, W.; Zhang, J.; Du, R.; Li, B.; Liu, W. Uncertainty analysis of photovoltaic cells to determine probability of functional failure. *Appl. Energy* **2023**, *332*, 120495. [CrossRef]
25. Zhang, F.; Han, C.; Wu, M.; Hou, X.; Wang, X.; Li, B. Global sensitivity analysis of photovoltaic cell parameters based on credibility variance. *Energy Rep.* **2022**, *8*, 7582–7588. [CrossRef]
26. Micheli, L.; Muller, M.; Theristis, M.; Smestad, G.P.; Almonacid, F.; Fernández, E.F. Quantifying the impact of inverter clipping on photovoltaic performance and soiling losses. *Renew. Energy* **2024**, *225*, 120317. [CrossRef]
27. Deline, C.; Muller, M.; White, R.; Perry, K.; Springer, M.; Deceglie, M.; Jordan, D. *Availability and Performance Loss Factors for U.S. PV Fleet Systems*; Technical Report NREL/TP-5K00-88769; National Renewable Energy Laboratory: Golden, CO, USA, 2024. [CrossRef]
28. Chen, X.; Li, B.; Braid, J.L.; Byford, B.; Colvin, D.J.; Glaws, A.; Jost, N.; Pierce, B.; Rabade, S.; Springer, M.; et al. Open data sets for assessing photovoltaic system reliability. *Appl. Energy* **2025**, *395*, 126132. [CrossRef]
29. Dhimish, M.; Vieira, R.; Poulsen, P.B. Reliability analysis of residential photovoltaic systems across five climatic zones: Performance, degradation, and fault trends. *Energies* **2025**, *18*, 6125. [CrossRef]
30. Anderson, K.S.; Hansen, C.W.; Holmgren, W.F.; Jensen, A.R.; Mikofski, M.A.; Driesse, A. pvlib python: 2023 project update. *J. Open Source Softw.* **2023**, *8*, 5994. [CrossRef]
31. Jensen, A.R.; Anderson, K.S.; Holmgren, W.F.; Mikofski, M.A.; Hansen, C.W.; Boeman, L.J.; Loonen, R. pvlib iotools—Open-source Python functions for seamless access to solar irradiance data. *Sol. Energy* **2023**, *266*, 112092. [CrossRef]
32. Lindig, S.; Herz, M.; Ascencio-Vásquez, J.; Theristis, M.; Herteleer, B.; Deckx, J.; Anderson, K.S. Review of technical photovoltaic key performance indicators and the importance of data quality routines. *Sol. RRL* **2024**, *8*, 2400634. [CrossRef]
33. Lindig, S.; Moser, D.; Curran, A.J.; Rath, K.; Khalilnejad, A.; French, R.H.; Herz, M.; Müller, B.; Makrides, G.; Georghiou, G.; et al. International collaboration framework for the calculation of performance loss rates: Data quality, benchmarks, and trends (towards a uniform methodology). *Prog. Photovolt. Res. Appl.* **2021**, *29*, 573–602. [CrossRef]

34. Fan, H.; Fu, S.; Ji, F.; Ma, L.; Wang, Y.; Sun, Y. A fast and effective method for reliability assessment of PV inverter. *Int. J. Electr. Power Energy Syst.* **2026**, *174*, 111518. [CrossRef]
35. Francisti, J.; Fodor, K.; Balogh, Z.; Magdin, M. Predictive modeling and anomaly detection in solar PV inverters using machine learning. *Results Eng.* **2025**, *28*, 108348. [CrossRef]
36. Liu, Y.; Duran, E.; Bruce, A.; Yildiz, B.; Severiano, B.M.; Ibrahim, I.A.; Rispler, J.; Martell, C.; Rougieux, F. A methodological review of cost-effective data-driven fault detection and diagnosis in distributed photovoltaic systems. *Appl. Energy* **2025**, *401*, 126636. [CrossRef]
37. Alawasa, K.M.; Al-Badi, A.H. Investigation and Analysis of the Power Quality in an Academic Institution's Electrical Distribution System. *Energies* **2024**, *17*, 3998. [CrossRef]
38. Atsu, D.; Seres, I.; Farkas, I. Power quality assessment and compliance of grid-connected PV systems in low voltage networks using microinverters. *Energy Syst.* **2026**, *17*, 551–582. [CrossRef]
39. *IEC 61683:1999*; Photovoltaic Systems—Power Conditioners—Procedure for Measuring Efficiency. International Electrotechnical Commission: Geneva, Switzerland, 1999.